

## Article

# The Iterative Extraction of the Boundary of Coherence Region and Iterative Look-Up Table for Forest Height Estimation Using Polarimetric Interferometric Synthetic Aperture Radar Data

Zenghui Huang <sup>1,2,3</sup> , Ye Yun <sup>1,2</sup>, Huiming Chai <sup>1,2</sup> and Xiaolei Lv <sup>1,2,3,\*</sup> 

<sup>1</sup> Key Laboratory of Technology in Geo-Spatial Information Processing and Application System, Aerospace Information Research Institute, Chinese Academy of Sciences, Beijing 100190, China; huangzenghui20@mails.ucas.ac.cn (Z.H.); yunye@aircas.ac.cn (Y.Y.); chaihm@aircas.ac.cn (H.C.)

<sup>2</sup> Aerospace Information Research Institute, Chinese Academy of Sciences, Beijing 100094, China

<sup>3</sup> School of Electronic, Electrical and Communication Engineering, University of Chinese Academy of Sciences, Beijing 100049, China

\* Correspondence: academism2017@sina.com or lvxl@aircas.ac.cn

**Abstract:** In this paper, we introduce a refined three-stage inversion algorithm (TSIA) for forest height estimation using polarimetric interferometric synthetic aperture radar (PolInSAR). Specifically, the iterative extraction of the boundary of the coherence region (IEBCR) and iterative look-up table (ILUT) are proposed to improve the efficiency of traditional TSIA. A class of refined TSIA utilizes the boundary of the coherence region (BCR) to alleviate the underestimation phenomenon in forest height estimation. Given many eigendecompositions in the extraction of BCR (EBCR), we analyze the relationship of eigenvectors between the adjacent points on the BCR and propose the IEBCR utilizing the power methods. In the final inversion stage of TSIA, the look-up table (LUT) uses the exhaustive search method to minimize the loss function in the 2-D grid with defined step sizes and thus costs high computational complexity. To alleviate the deficiency, we define the random volume over ground (RVoG) function based on the RVoG model and prove its monotonicity and convergence from the analytical and numerical points of view. After analyzing the relationship between the RVoG function and the loss function, we propose the ILUT for the inversion stage. The simulation and experiments based on the BioSAR 2008 campaign data illustrate that the IEBCR and ILUT greatly improve the computational efficiency almost without compromising on accuracy.



**Citation:** Huang, Z.; Yun, Y.; Chai, H.; Lv, X. The Iterative Extraction of the Boundary of Coherence Region and Iterative Look-Up Table for Forest Height Estimation Using Polarimetric Interferometric Synthetic Aperture Radar Data. *Remote Sens.* **2022**, *14*, 2438. <https://doi.org/10.3390/rs14102438>

Academic Editors: Thomas Alexandridis, Christos Chalkias, Konstantinos X. Soulis, Dionissios Kalivas and Emmanouil Psomadias

Received: 11 April 2022

Accepted: 17 May 2022

Published: 19 May 2022

**Publisher's Note:** MDPI stays neutral with regard to jurisdictional claims in published maps and institutional affiliations.



**Copyright:** © 2022 by the authors. Licensee MDPI, Basel, Switzerland. This article is an open access article distributed under the terms and conditions of the Creative Commons Attribution (CC BY) license (<https://creativecommons.org/licenses/by/4.0/>).

## 1. Introduction

Forest height is a pivotal parameter in biomass estimation which plays an essential role in forest management, biodiversity, global carbon storage, and climate modeling [1–4]. Remote sensing technologies can provide a means for large-scale forest height measurement. There are mainly three forest height inversion methods in remote sensing technologies.

The first method is Light Detection and Ranging (LiDAR). LiDAR can measure the three-dimensional physical distribution of the forest canopy directly, thus providing the most accurate estimates of forest height compared with other remote sensing techniques [5]. Therefore, the LiDAR-derived height is often used to validate the reliability of other remote sensing techniques. However, the large-scale tree height retrieval based on LiDAR is limited by the high acquisition cost [6].

The second approach is the model-based inversion. In recent decades, the PolInSAR technology has shown great potential in forest height inversion. Extensive research has demonstrated that the forest height can be estimated from PolInSAR data at X-, C-, L-, and P-bands [7–20].

The third method is based on machine learning, including decision trees ensemble methods and support vector machine [21,22]. In the model-based methods, the relationship between the observations and the forest structure parameters is complex and nonlinear. More parameters describing the scattering process usually generate a better inversion result. However, the nonlinear models are often ill-posed [23,24]. Therefore, some scholars have tried to use machine learning methods to estimate the forest height [6,25–27]. However, the performance of these algorithms highly depends on the training samples [6]. Moreover, the training process requires lots of PolInSAR and LiDAR data, which limits the application of this method.

In this paper, we mainly focus on the model-based inversion methods. This study estimates the forest heights from the PolInSAR data according to the inversion methods. The LiDAR canopy heights are used for comparison and validation of inverted forest heights. RVoG model is one of the most widely used models among these methods [28–30]. The model assumes that the canopy is a uniform particles layer with random directions. The observed coherence is modeled in terms of four physical parameters: the forest height, which denotes the thickness of the canopy; the mean extinction coefficient, which indicates the attenuation of the electromagnetic waves through the canopy; the ground phase relating to the underlying topography; and the ground-to-volume amplitude ratio (GVR), which varies with the polarization channels.

The three-stage inversion algorithm (TSIA) was proposed based on the geometrical characteristics of the RVoG model [31]. The geometrical characteristic avoids the six-dimensional nonlinear optimization problem and reduces the computational complexity [7,31]. Concretely, a coherence line is firstly fitted by the least squares using the observed coherences. Combining the NGVR hypothesis, the ground phase is estimated for each pixel in the second stage. Finally, the look-up table is established for the remaining parameters, height, and extinction.

The traditional TSIA has two limitations. On the one hand, the TSIA uses several observed coherences to fit the coherence line and estimate the ground phase. However, the observed coherences can be influenced by various parameters, including temporal or spatial baseline, frequency, and systematic errors. Therefore, the coherence line is not robust enough and cannot fully reflect the characteristics of the entire coherence region. On the other hand, the TSIA approximates the volume coherence with HV polarization coherence resulting in the underestimation phenomenon.

Based on the boundary of the coherence region (BCR) [32], some coherence optimization algorithms have been proposed, including the phase diversity algorithm [33], magnitude difference algorithm [34], numerical radius algorithm [35], and principal component analysis of coherence region [36]. In addition, some refined three-stage inversion algorithms [36,37] have been proposed using these coherence optimization algorithms. In the direction of the fitted coherence line, the boundary points are regarded as the coherences with the largest and smallest GVR. The coherence with minimum GVR is the best candidate for the volume-only coherence. Two computational burdens make these refined algorithms a time-consuming process that is intolerable in practice. For one thing, the computation is enormous, as many eigendecompositions need to be solved for each pixel in the EBCR. For another thing, in the final inversion stage, the look-up table (LUT) uses the exhaustive search method to minimize the loss function in the 2-D grid with defined step sizes and thus costs high computational complexity.

In this paper, we try to enhance the efficiency of the refined TSIA. To achieve this, we study the eigenvectors of the adjacent points and utilize the power methods to improve the computational efficiency, which avoids the eigendecompositions. Moreover, we define the RVoG function based on the RVoG model. Then, we prove its monotonicity and convergence from the analytical and numerical points of view. After analyzing the relationship between the RVoG function and the loss function, we propose an iterative LUT (ILUT) for the inversion problem.

This article is organized as follows. Section 2 presents the basic processing flow of the model-based PolInSAR inversion. Section 3 introduces the proposed iterative methods.

Section 4 concerns the experimental results. Section 5 presents the discussion on the further analysis of the iterative methods. Finally, conclusions are given in Section 6.

## 2. Model-Based Pol-InSAR Inversion

The basic flow of PolInSAR inversion can be divided into three parts, namely PolInSAR observation, modeling, and inversion [11].

### 2.1. Observation

The PolInSAR data is obtained from two separate antennas in different positions or times. For a single-baseline PolInSAR system, the Pauli scattering vectors of the two registered images are [23]

$$\begin{aligned} k_1 &= \frac{1}{\sqrt{2}} [ s_{hh_1} + s_{vv_1} \quad s_{hh_1} - s_{vv_1} \quad 2s_{hv_1} ]^T \\ k_2 &= \frac{1}{\sqrt{2}} [ s_{hh_2} + s_{vv_2} \quad s_{hh_2} - s_{vv_2} \quad 2s_{hv_2} ]^T \end{aligned} \quad (1)$$

where  $k_1, k_2$  are the Pauli scattering vectors from the pixel of two images assuming target reciprocity ( $s_{hv_i} = s_{vh_i}$ ), the subscripts 1,2 denote master and slave, respectively, the superscript  $(\cdot)^T$  denotes the transpose,  $s_{hh_i}, s_{vv_i}, s_{hv_i}, i = 1, 2$  are the backscatter coefficient from different polarization channels, and the subscripts  $h$  and  $v$  indicate the horizontal polarization and vertical polarization, respectively.

The coherence matrix and polarimetric interferometric matrix are computed from

$$\begin{aligned} T_i &= \frac{1}{2} \langle k_i k_i^H \rangle, i = 1, 2 \\ \Omega &= \frac{1}{2} \langle k_1 k_2^H \rangle \end{aligned} \quad (2)$$

where  $T_1, T_2$  are the Hermitian coherence matrix, the superscript  $(\cdot)^H$  denotes the conjugate transpose,  $\langle \cdot \rangle$  indicates the ensemble average in order to reduce bias [38], and  $\Omega$  is the polarimetric interferometric matrix.

Complex coherence can be introduced according to the unitary complex projection vectors [30,32]

$$\gamma(w) = \frac{w^H \Omega w}{w^H T w} \quad (3)$$

where  $T = \frac{1}{2}(T_{11} + T_{22})$  and  $\gamma$  is the interferometric coherence relating to the projection vectors  $w$ . In real data processing,  $T_1$  and  $T_2$  are close. Adding up the two matrices is reasonable because the assumption of polarization stability is valid in most cases [23,32].

### 2.2. RVoG Model

The purpose of modeling is to link the observed coherences with the physical parameters. The complex coherence  $\gamma_{g,v}(w)$  [23] in the RVoG model is

$$\gamma_{g,v}(w) = \frac{\mu}{\mu + 1} e^{jk_z z_0} + \frac{1}{\mu + 1} \gamma_v \quad (4)$$

where the subscripts  $g, v$  mean two contributions from the ground surface and the canopy (often referred to as volume),  $z_0$  is the ground height,  $\mu$  presents the GVR,  $w$  indicates the unitary complex projection vector relating to the polarization,  $j$  illustrates the imaginary unit,  $\gamma_v$  denotes the pure volume coherence, and the vertical wavenumber  $k_z$ .  $k_z$  and  $\gamma_v$  [23,31] are defined as follows

$$k_z = \frac{4\pi\Delta\theta}{\lambda \sin\theta} \quad (5)$$

$$\gamma_v(h_v, k_e) = e^{j\varphi_g} \frac{p_1}{p_2} \frac{e^{p_2 h_v} - 1}{e^{p_1 h_v} - 1} \quad (6)$$

where  $h_v$  is the forest height,  $k_e$  indicates the mean wave extinction coefficient,  $\theta$  presents the mean angle of incidence,  $\Delta\theta$  indicates the difference of  $\theta$  between antennas, and the wavelength  $\lambda$ .  $p_1, p_2$  are defined as follows for convenience

$$p_1 = \frac{2k_e}{\cos \theta}, p_2 = p_1 + jk_z \quad (7)$$

According to the normalization in Equation (3), the complex coherence is located in the unit circle of the 2-D complex plane. Equation (4) indicates that the complex coherence is the convex combination of ground coherence  $e^{jk_z z_0}$  and volume coherence  $\gamma_v$ . Therefore, the complex coherence is located on the line segment that links  $e^{jk_z z_0}$  and  $\gamma_v$ .

### 2.3. Refined Three-Stage Inversion Scheme

Figure 1 presents the basic PolInSAR flow. The observation in PolInSAR is the coherence that is obtained after a series of preprocessing. The RVoG model is the bridge linking observation and inversion. To estimate the forest height from the PolInSAR observation and RVoG model, the inversion scheme is divided into three stages, namely coherence line fitting according to the IEBCR method, volume coherence and ground phase estimation, and height and extinction estimation in the ILUT method.

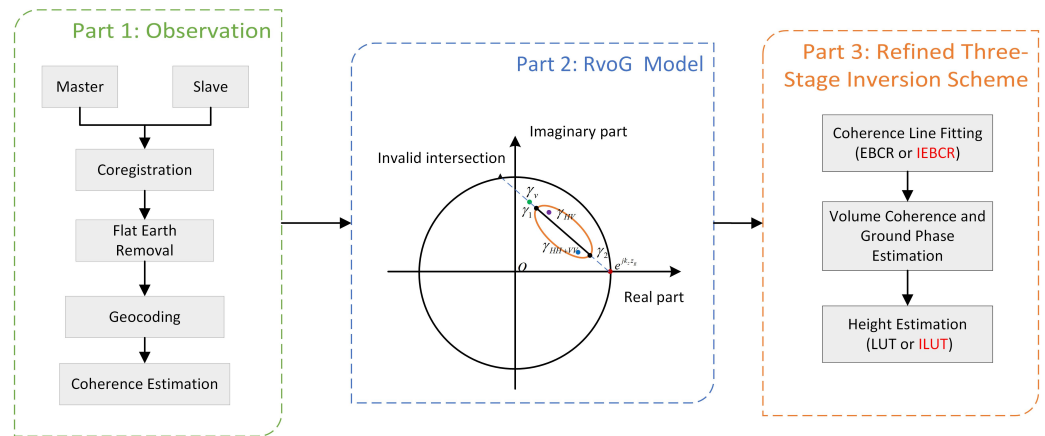


**Figure 1.** The PolInSAR flow. The figure in Part 2 depicts the geometrical interpretation of the RVoG model in the unit circle. The orange ellipse is the locus of BCR. The green, purple, blue, and red points are volume coherence, HV polarization coherence, HH+VV polarization coherence, and ground coherence, respectively. The black points denote two candidates of the volume coherence with the largest and smallest GVR, respectively. The blue dotted line linking  $\gamma_v$  and  $e^{jk_z z_0}$  is the theoretical distribution of coherence based on the RVoG model. The solid line over the blue dotted line is the visible segment. The black triangle is the invalid intersection.

#### 2.3.1. Coherence Line Fitting

The IEBCR method is first implemented to generate the boundary coherence. As shown in Figure 1, in the principal direction of the BCR, the boundary points  $\gamma_1, \gamma_2$  are regarded as the coherence with the largest and smallest GVR [36,39]. Therefore, the line passing through these two points is the optimal coherence line.

#### 2.3.2. Volume Coherence and Ground Phase Estimation

In the complex plain, the ground coherence is one of the intersections between the coherence line and the unit circle. The HH+VV polarization  $\gamma_{HH+VV}$  generally has a higher

GVR than the HV polarization  $\gamma_{HV}$  [31]. Therefore, the criterion to determine the volume coherence is as follows [31,36]

$$(\gamma_h, \gamma_l) = \begin{cases} (\gamma_1, \gamma_2), & \text{if } |\gamma_1 - \gamma_{HV}| < |\gamma_1 - \gamma_{HH+VV}| \\ (\gamma_2, \gamma_1), & \text{otherwise.} \end{cases} \quad (8)$$

With the volume coherence, the ground phase can be estimated from the two intersections in return

$$\phi_0 = \begin{cases} \phi_1, & \text{if } |e^{j\phi_1} - \gamma_l| < |e^{j\phi_1} - \gamma_h| \\ \phi_2, & \text{otherwise.} \end{cases} \quad (9)$$

where  $\phi_0$  indicates the ground phase,  $e^{j\phi_1}, e^{j\phi_2}$  are the two intersections between the coherence line and the unit circle, and  $|\cdot|$  denotes the Euclidean distance.

### 2.3.3. Height and Extinction Estimation

Assuming that the estimated  $\gamma_h$  satisfies the NGVR assumption, the height and extinction can be estimated according to the 2-D LUT, which is based on Equation (6) [31]

$$\tilde{h}_v = \arg \min_{h_v, k_e} |\gamma_h - \gamma_v(h_v, k_e)| \quad (10)$$

where  $\tilde{h}_v$  denotes the estimated height and  $h_v, k_e$  vary in the 2-D solution space. As shown in Figure 1, the ILUT is applied to solve the optimization problem.

## 3. Methods

### 3.1. IEBCR

The maximum and minimum real part of  $\gamma$  correspond to the generalized Rayleigh quotient problem, which can be transformed to the following eigendecomposition problems [40]

$$\begin{aligned} A_k w &= \lambda T w \\ A_k &= \frac{1}{2} \left( \Omega e^{i\phi_k} + \Omega^H e^{-i\phi_k} \right) \\ \phi_k &= 2k\pi/N, 1 \leq k \leq N/2 \end{aligned} \quad (11)$$

where  $A_k$  and  $T$  are  $3 \times 3$  Hermitian matrices,  $\phi_k$  denotes the angle of phase rotation, and  $N$  is the number of the boundary points. For each  $\phi_k$ , the eigendecomposition yields two extreme values of the real part of  $\gamma$ , which correspond to the maximum and minimum eigenvalues. A pair of coherences can be estimated using the corresponding eigenvectors according to Equation (3). The accuracy of EBCR depends on the step of the sampled angle. As long as the phase spacing is small enough, the EBCR is accurate.

To extract the BCR, a series of eigendecompositions for each pixel in Equation (11) is a time-consuming task. The problem can be arranged as follows

$$\begin{aligned} T^{-1} A_k w_k &= \lambda_k w_k \\ T^{-1} A_{k+1} w_{k+1} &= \lambda_{k+1} w_{k+1} \end{aligned} \quad (12)$$

The relationship between eigenvectors is the key to calculating the coherence

$$w_{k+1} = f(w_k, \Delta\phi) \quad (13)$$

where the angle  $\Delta\phi$  is the phase spacing. Since the matrix multiplication corresponds to the linear transformation, we can focus on the relation between  $A_k$  and  $A_{k+1}$ . In some particular cases, there are some good properties on the eigendecomposition problem between a matrix and its Hermitian part [41,42]. The difficulties of finding the analytical form arise from  $\Omega$  which does not provide the special properties. Therefore, we attempt to use the numerical relation instead.

Multiplying a matrix by the term  $e^{j\phi}$  corresponds to the rotation. After rotating, the eigenvectors of matrix  $\Omega$  become the eigenvectors of the matrix  $e^{j\phi}\Omega$ . Because the angle  $\Delta\phi$  is small, the change from  $\Omega$  to  $e^{j\phi}\Omega$  is rather small. As we mentioned before,  $A_k$  is the Hermitian part of  $\Omega$ , and  $A_{k+1}$  is the Hermitian part of  $e^{j\phi}\Omega$ . We infer that the eigenvectors of  $A_k$  and  $A_{k+1}$  are close.

Figure 2 presents the relationship between the eigenvectors. The figure illustrates that the eigenvectors corresponding to the similar eigenvalue are close. To avoid the eigendecompositions, we use the relation in power methods to compute the eigenvectors [43].

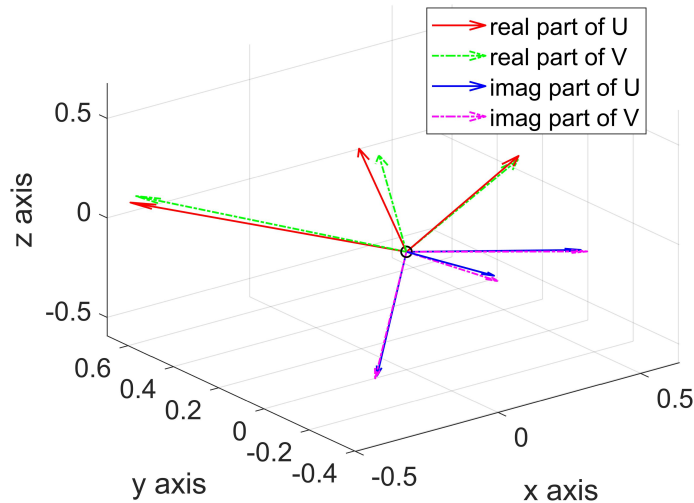


**Figure 2.** The example of the eigenvectors.  $U$  is the eigenvector matrix of  $T^{-1}A_k$  and  $V$  is the eigenvector matrix of  $T^{-1}A_{k+1}$ . The eigenvectors are the columns of  $U$  and  $V$ . The arrows denote the eigenvectors in the 3-D plot.

Assuming the matrix  $B \in \mathbb{C}^{n \times n}$  has  $n$  linearly independent eigenvectors  $v_i, i = 1, 2, \dots, n$  and eigenvalues  $\lambda_i, i = 1, 2, \dots, n$

$$Bv_i = \lambda_i v_i, |\lambda_1| \geq |\lambda_2| \geq \dots \geq |\lambda_n|$$

The power method starts from a vector  $b_0$ , which can be a random vector or an approximation of the dominant eigenvector of the matrix. The method can be written as follows [43]

$$b_{k+1} = Bb_k \quad (14)$$

The vector  $b_k$  is multiplied by  $B$  at each iteration. These linearly independent eigenvectors form a basis of  $n$ -dimensional space. Therefore,  $b_0$  can be written as a linear combination of the  $n$  eigenvectors

$$b_0 = \sum_{i=1}^n \alpha_i v_i \quad (15)$$

Thus  $b_1 = Bb_0 = \sum_{i=1}^n \alpha_i \lambda_i v_i$ . Generally

$$b_{k+1} = Bb_k = \sum_{i=1}^n \alpha_i \lambda_i^k v_i = \lambda_1^k \sum_{i=1}^n \alpha_i \left( \frac{\lambda_i}{\lambda_1} \right)^k v_i \quad (16)$$

For sufficiently large  $k$ ,

$$\left| \frac{\lambda_i}{\lambda_1} \right|^k \rightarrow 0$$

So, we have

$$b_{k+1} \approx \lambda_1^k \alpha_1 v_1$$

The eigenvalue and eigenvector can be computed from

$$\lambda_1 \approx b_{k+1}^{(1)} / b_k^{(1)}, v_1 \approx b_{k+1} \quad (17)$$

Taking the arithmetic overflow into consideration, the normalization is usually performed in actual calculation. Thus, the iteration can be written as

$$b_{k+1} = \frac{Bb_k}{\|Bb_k\|} \quad (18)$$

The power method converges to the eigenvector corresponding to the eigenvalue with the largest amplitude. The least eigenvalue in amplitude can be obtained by the inverse power method.

In our problem, the eigenvalue must be real because  $T, A_k$  are Hermitian matrices. The boundary points on the BCR correspond to the largest and smallest eigenvalues. However, the power methods can only obtain the largest and least eigenvalues in amplitude. As the eigenvalues are sorted differently, the eigenvectors are not always identical. Figure 3 illustrates two cases in eigenvalue sorting. In the first case, the eigendecomposition and the power methods get the same eigenpairs. However, in Case 2, they are different. To solve this problem, we use a theorem as follows

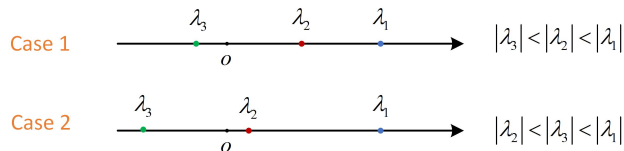


**Figure 3.** The different sorting cases of eigenvalues.

**Theorem 1 ([44]).** Let  $p(t)$  be a given polynomial of degree  $k$ . If  $(\lambda, x)$  is an eigenvalue–eigenvector pair of  $B \in C^{n \times n}$ , then  $(p(\lambda), x)$  is an eigenvalue–eigenvector pair of  $p(B)$ .

Therefore, a proper identity matrix can be added to change the eigenvalues while the eigenvectors remain unchanged

$$\tilde{B} = B + \theta I \quad (19)$$

Note that the coefficient  $\theta$  is of importance. On the one hand,  $\theta$  should ensure that all the eigenvalues of  $\tilde{B}$  are positive. On the other hand, the identity matrix should not change the relationship between  $A_k$  and  $A_{k+1}$ . For example, if  $\theta$  is large enough, the matrix  $\tilde{B}$  becomes a diagonally dominant matrix leading to the failure of the phase rotations algorithm. The spectral radius of a square matrix is the largest absolute value of its eigenvalues [44]

$$\rho(B) = \max |\lambda_B| \quad (20)$$

$\rho(B)$  precisely satisfies the requirement of  $\theta$ . However, computing the spectral radius is also an eigendecomposition work. The spectral radius is the lower bound of any norm of matrix [44], so we use the 2-norm.

After a series of transformations, the orders of eigenvalues are consistent. To keep notation light, we rewrite the problem

$$\begin{aligned} B_0 &= T^{-1}(\Omega + \Omega^H) \\ B_k &= T^{-1}(e^{j\phi_k}\Omega + e^{-j\phi_k}\Omega^H) \end{aligned}$$

Since the eigenvectors of  $B$  and  $\tilde{B}$  are close, the eigenvectors of  $B_k$  are set as the initial vector of power methods in solving eigenvectors of  $B_{k+1}$ . The power methods can reach high accuracy after several iterations. The IEBCR is summarized in Algorithm 1.

**Algorithm 1** IEBCR.

---

```

1: Input: The polarimetric interferometric matrix  $\Omega$ , the coherence matrix  $T$ , the phase
   step  $\phi$ 
2: Output: The boundary coherence vector  $\gamma \in \mathbb{C}^{2n}$ 
   % main procedure: %
3: Eigendecomposition of  $B_0 = T^{-1}(\Omega + \Omega^H)$ 
4: Sort the eigenvalues,  $\lambda_1 > \lambda_2 > \lambda_3$ , with eigenvectors  $v_1, v_2, v_3$ . Calculate  $\gamma_1, \gamma_2$ 
   according to Equation (3) using  $v_1, v_2$ .
5: Calculate the spectral norm of  $B_0$ ,  $\theta = \|B_0\|_2$ .
6: % main loop: %
7: for  $k = 2 : n$  do
8:    $B_k = T^{-1}(e^{jk\phi}\Omega + e^{-jk\phi}\Omega^H)$ 
9:    $\tilde{B}_k = B_k + \theta I$ 
10:   $v_1 = \text{Power Method } (v_1, \tilde{B}_k)$ 
11:   $v_3 = \text{Inverse Power Method } (v_3, \tilde{B}_k)$ 
12:   $\gamma_{2k-1} = v_1^H \Omega v_1 / v_1^H T v_1$ 
13:   $\gamma_{2k} = v_3^H \Omega v_3 / v_3^H T v_3$ 
14:   $k = k + 1$ 
15: end loop

```

---

In the algorithm, the 2-norm is not calculated in each iteration. First, calculating the 2-norm in each iteration is time-consuming. More importantly, using the norm of  $B_0$  is feasible in actual calculations.

### 3.2. ILUT

In the final stage of TSIA, the exhaustive search strategy to get the optimal parameters in the defined step sizes brings high computational complexity. To explore the property of loss function in Equation (10), we define the RVoG function as follows

$$f = \left| \frac{p_1}{p_2} \frac{e^{p_2 h_v} - 1}{e^{p_1 h_v} - 1} \right|^2 \quad (21)$$

From the function plots in Figure 4, the function seems to have the following characteristics.

1. For a fixed  $k_e$ , the function converges to a value as the tree height increases. Moreover, the value increases with the increase of  $k_e$ .
2. In the direction of  $h_v$ , the function is monotonically decreasing in a specific interval.
3. In the direction of  $k_e$ , the function is monotonically increasing.

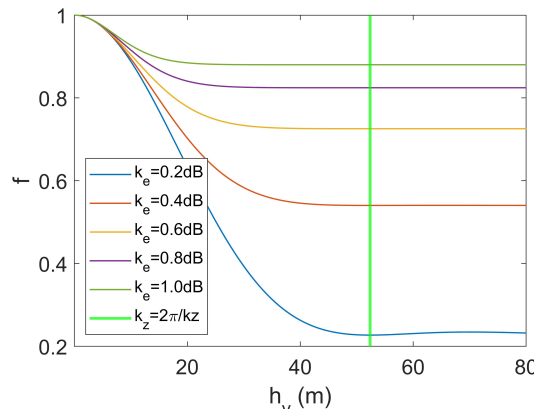


**Figure 4.** The RVoG function with  $\theta = \pi/4, k_z = 0.12 \text{ m}^{-1}$ .

In the following text, we will attempt to prove these properties from analytic and numerical points of view.

### 3.2.1. Convergence Properties

The linear relationship between  $p_1$  and  $k_e$  does not influence the characteristics of the function. For convenience, we use  $p_1$  to represent  $k_e$  in proving text. To illustrate the convergence, we simplify  $f$  using Euler's formula as follows

$$\begin{aligned} f &= \left| \frac{p_1}{p_1 + jk_z} \right|^2 \left| \frac{e^{p_1 h_v} e^{jk_z h_v} - 1}{e^{p_1 h_v} - 1} \right|^2 \\ &= \frac{p_1^2}{p_1^2 + k_z^2} \left( 1 + 2 \frac{e^{p_1 h_v}}{(e^{p_1 h_v} - 1)^2} (1 - \cos(k_z h_v)) \right) \end{aligned} \quad (22)$$

The first part is independent of  $h_v$ . When  $h_v$  is sufficiently large, we have

$$\begin{aligned} &= \lim_{h_v \rightarrow \infty} \frac{p_1^2}{p_1^2 + k_z^2} \left( 1 + 2 \frac{e^{p_1 h_v}}{(e^{p_1 h_v} - 1)^2} (1 - \cos(k_z h_v)) \right) \\ &= \frac{p_1^2}{p_1^2 + k_z^2} \end{aligned} \quad (23)$$

The above expression is monotonically increasing with  $p_1$ . Moreover, as  $p_1$  operates on the exponential term, the curve converges faster when  $p_1$  is larger.

We next prove that the minimum value of the function is the convergence value.

The second part of  $f$  has a concise geometric interpretation as shown in Figure 5. According to the triangle inequality, the difference between any two sides of a triangle must less than the length of the third side. So, the length of the orange vector is larger than that of the green vector. So, we have

$$\left| \frac{e^{p_1 h_v + jk_z h_v} - 1}{e^{p_1 h_v} - 1} \right| > 1 \Rightarrow f > \frac{p_1^2}{p_1^2 + k_z^2} \quad (24)$$

Moreover,

$$f\left(\frac{2n\pi}{k_z}\right) = \frac{p_1^2}{p_1^2 + k_z^2}, n = 1, 2, \dots \quad (25)$$

where  $2n\pi/k_z$  is the ambiguity height. It demonstrates that the inversion capability of the RVoG model is  $[0, 2\pi/k_z]$ . Therefore, we infer that the monotonic interval in the  $h_v$  direction is  $[0, 2\pi/k_z]$ . Next, we will prove the monotonicity of  $f$  in both directions.

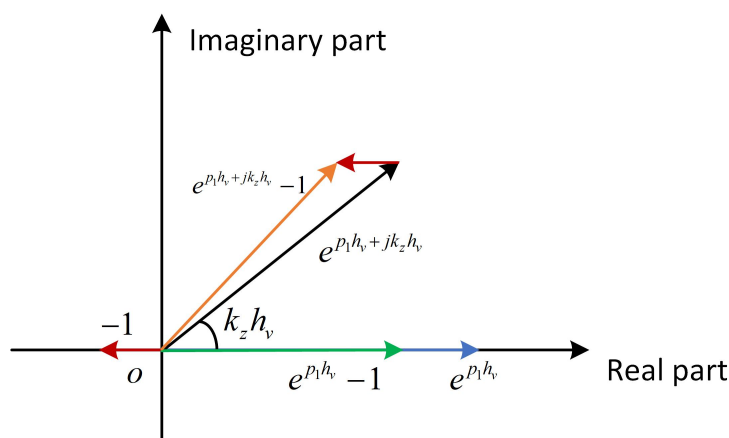


**Figure 5.** Geometric interpretation of the second part of the RVoG function. The blue vector denotes  $e^{p_1 h_v}$ . After rotating a angle of  $k_z h_v$ ,  $e^{p_1 h_v}$  becomes  $e^{p_1 h_v + jk_z h_v}$  denoted by the black vector. The red vector is  $-1$ . The green vector presents  $e^{p_1 h_v} - 1$ . The orange vector denotes  $e^{p_1 h_v + jk_z h_v} - 1$ , which is the vector sum of  $e^{p_1 h_v + jk_z h_v}$  and  $-1$ .

### 3.2.2. Monotonicity

The partial derivative of the RVoG function with respect to  $h_v$  is

$$\frac{\partial f}{\partial h_v} = \frac{p_1^2 e^{p_1 h_v}}{(p_1^2 + k_z^2)(e^{p_1 h_v} - 1)^3} \left\{ k_z \sin(k_z h_v) (e^{p_1 h_v} - 1) - p_1 [1 - \cos(k_z h_v)] (e^{p_1 h_v} + 1) \right\} \quad (26)$$

Apparently, the ambiguity heights are the stationary points that satisfy the following equation

$$\frac{\partial f}{\partial h_v} \left( \frac{2n\pi}{k_z} \right) = 0, n = 1, 2, \dots \quad (27)$$

It is challenging to determine whether there are other stationary points because of the exponential and trigonometric terms. For a fixed  $h_v$ , the derivative changes with  $p_1$  and  $k_z$ , and we can judge its sign according to the numerical computation. However, we can not exhaust all  $h_v$  in the range of  $[0, 2\pi/k_z]$  to prove the monotonicity. To achieve this goal, we carry out the following transformation

$$t = p_1/k_z, x = k_z h_v, 0 < x < 2\pi \quad (28)$$

With the transformation, the derivative function has two variables left and can be written as

$$\frac{\partial f}{\partial x} \sim \frac{t^2}{t^2 + 1} \frac{e^{tx}}{(e^{tx} - 1)^3} [(e^{tx} - 1) \sin x - t(1 - \cos x)(e^{tx} + 1)] \quad (29)$$

Figure 6a provides the contour map of the derivative function. The derivative function is always negative, which means the function  $f$  is monotonically decreasing in  $[0, 2\pi/k_z]$ .

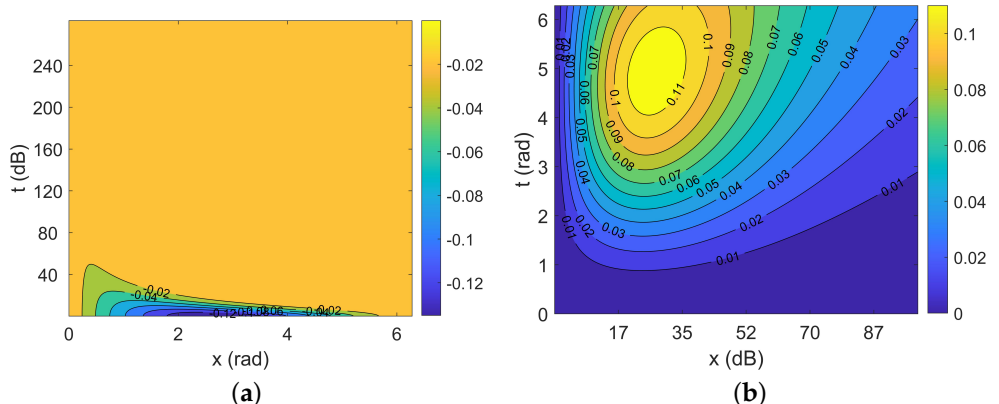


**Figure 6.** The contour of the partial derivative of the RVoG function.  $k_e$  ranges between 0 and 1 dB/m [14], and  $k_z > 0.01 \text{ m}^{-1}$ ,  $\theta = \pi/4$ . (a) Direction of  $h_v$ . (b) Direction of  $p_1$ .

The partial derivative of the RVoG function with respect to  $p_1$  can be written as follows

$$\frac{\partial f}{\partial p_1} = \frac{p_1}{p_1^2 + k_z^2} \left[ \frac{2k_z^2}{p_1^2 + k_z^2} + \frac{2(1 - \cos(k_z h_v))e^{p_1 h_v}}{(e^{p_1 h_v} - 1)^2} \cdot \left( \frac{2k_z^2}{p_1^2 + k_z^2} - p_1 h_v \frac{e^{p_1 h_v} + 1}{e^{p_1 h_v} - 1} \right) \right] \quad (30)$$

Similarly, in order to explain the sign of the derivative more conveniently, we apply the following transformation

$$x = p_1 h_v, t = k_z h_v, 0 < t < 2\pi \quad (31)$$

So, the derivative becomes

$$\frac{\partial f}{\partial x} \sim \frac{2xt^2}{(x^2 + t^2)^2} \left[ 1 + \frac{2e^x}{(e^x - 1)^2} (1 - \cos t) \right] - \frac{2(1 - \cos t)x^2}{x^2 + t^2} \frac{e^x(e^x + 1)}{(e^x - 1)^3} \quad (32)$$

Figure 6b presents the contour of the derivative. The positive derivative demonstrates that  $f$  is monotonically increasing in the  $p_1$  direction.

### 3.2.3. ILUT

The RVoG function and loss function have different geometric interpretations despite similar forms. In the 2-D complex plane, the loss function denotes the Euclidean distance between the calculated coherence and the observed coherence. The RVoG function denotes the Euclidean distance between the theoretical coherence and the origin.

Figure 7 shows the geometrical representation and the contour of the loss function. The black rectangles indicate the neighborhood near the optimal solution. In the complex space, the neighborhood has a rather small distance that corresponds to the blue band areas in the contour map. After analysis, the optimization problem does not exhibit particularly irregular properties. Therefore, as long as the neighborhood of the optimal solution can be found in the initial search, a new grid can be established locally to get a better solution. Figure 7 inspires us that the iterative LUT (ILUT) can be established in the inversion process. Specifically, a coarse grid is first established to search the neighborhood near the optimal solution, then a series of refined grids can be established in the neighborhood for the optimal solution. Algorithm 2 provides the details of ILUT.

Moreover, the loss function is more sensitive in the direction of  $h_v$  than that of  $k_e$ . Therefore, in the contour map, blue band areas appear near the optimal solution in the direction of  $k_e$ . Thus, a fixed extinction coefficient, assuming 0.4 dB/m, can still achieve reasonable inversion results despite the loss of accuracy. Some scholars have tried this during the inversion process [8,37], and our analysis verifies the rationality of this approach.

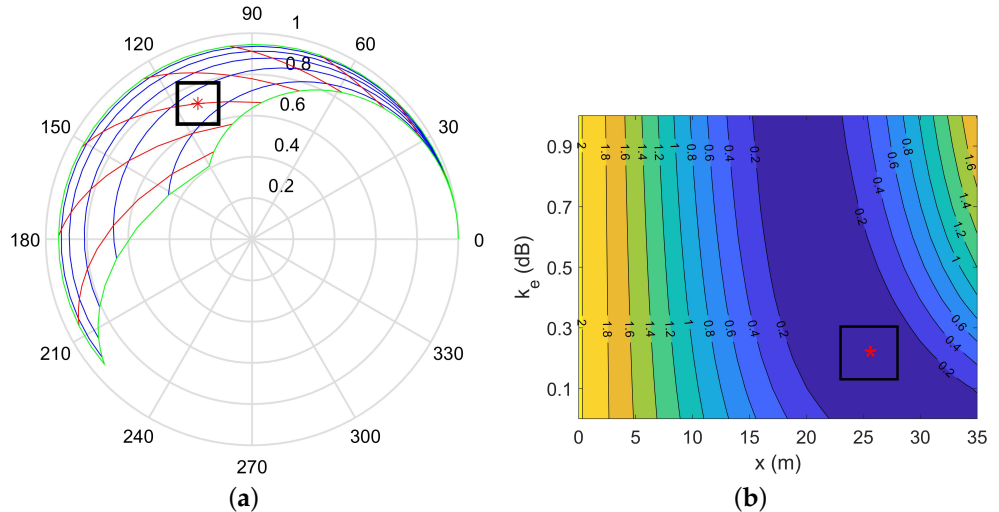


**Figure 7.** Different representation of the loss function with  $\theta = \pi/4, k_z = 0.12 \text{ m}^{-1}$ . The red asterisks denote the location of the observed coherence which is also the optimal solution. The black rectangles indicate the neighborhood near the optimal solution. (a) Geometrical representation of the loss function. The area enclosed by the green line is the solution space where the coherences are calculated by Equation (6). The blue line denotes the direction of  $h_v$ . The red line presents the direction of  $k_e$ . (b) The contour of the loss function.

**Algorithm 2** ILUT.

---

```

1: Input: The candidate of volume coherence  $\tilde{\gamma}_v$ , the range of  $k_e$ :  $k_{emax}, k_{emin}$ , the range of  $h_v$ :  $h_{vmax}, h_{vmin}$ , the precision  $\Delta k_e$  and  $\Delta h_v$ .
2: Output: The inversion height  $\tilde{h}_v, \tilde{k}_e$  and the loss function value loss
% main procedure:
3: The initial step  $\Delta h_{vi}, \Delta k_{ei}$ , the ratio of step m
4: % main loop: LUT inversion:  $h_{best}, k_{ebest}, loss$  %
5: while  $\Delta h_{vi} > \Delta h_v$ 
6:    $h_{vmin} = h_{best} - \Delta h_{vi}, h_{vmax} = h_{best} + \Delta h_{vi}$ 
7:    $k_{emin} = k_{best} - \Delta k_{ei}, k_{emax} = k_{best} + \Delta k_{ei}$ 
8:    $\Delta h_{vi} = \Delta h_{vi}/m$ 
9:    $\Delta k_{ei} = \Delta k_{ei}/m$ 
10: end loop

```

---

## 4. Results

### 4.1. Data Description

This paper uses European Space Agency (ESA) BioSAR 2008 data [45] to verify the effectiveness of the proposed algorithms. The data were acquired by the German Aerospace Center (DLR) E-SAR system in Northern Sweden. The test site is mainly confined within the Krycklan River catchment (KCS). The KCS is 6790 ha in area and comprises a mosaic of instrumented and well-studied forests, agriculture, wetlands, and lakes, all drained and connected by a network of streams and rivers [46]. Mixed coniferous forest is the dominating forest type, primarily between 0–35 m in height. The data contains airborne SAR data and the LiDAR H100 data. The SAR images are Single Look Complex (SLC) format with four polarization channels: HH, HV, VH and VV. The SAR data were acquired in two different flight directions with various spatial baselines. First flight direction is 313° with a southwest radar look direction. The other flight direction is 133° with the northeast radar look direction. Table 1 provides some details of the PolInSAR data. In this paper, the researched data is 6 m baseline at L-band and 24 m baseline at P-band. The reference height for validation is the LiDAR H100, which is defined as the mean height of the 100 highest trees per hectare [47]. Previous works have well demonstrated that the LiDAR H100 can provide precise measurement for forest canopy height [6,47].

**Table 1.** Characteristics of PolInSAR data.

Band	L	P
Centre Frequency	1.300 GHz	0.349 GHz
Spatial Baseline	6, 12, 18, 24, 30 m	8, 16, 24, 32, 40 m
Flight Direction		133° and 313°
Easting size		9561
Northing size		9821
Easting Range		437,061–446,881 m
Northing Range		7,119,733–7,129,293 m
Geocoded Resolution		1 m × 1 m

The coordinate system is the UTM Zone 34 coordinate.

Figure 8a shows the Pauli-basis polarimetric composite image. Figure 8b provides the LiDAR H100 forest height map. It is worth noting that the resolution of the LiDAR map and geocoded SAR images is 10 m × 10 m, 1 m × 1 m, respectively.

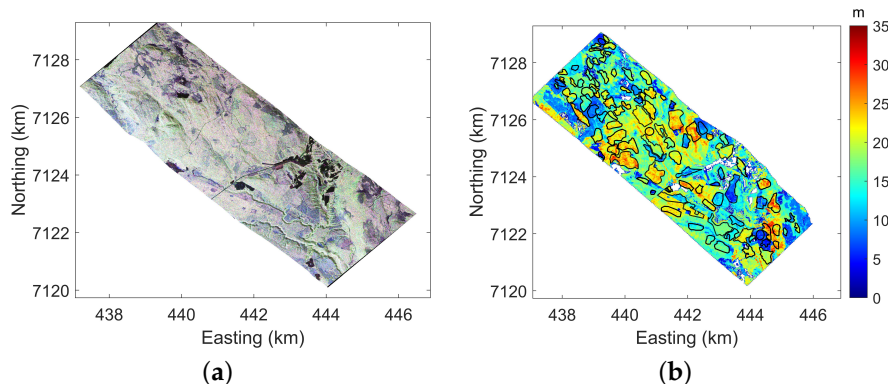


**Figure 8.** The Pauli-basis color composite map and LiDAR H100 height map. Both maps are defined in the UTM Zone 34 coordinate. (a) The Pauli-basis color composite map. (b) The LiDAR H100 height map. The polygons are used in the forest height validation. The color ramp ranges from 0 to 35 m.

#### 4.2. Evaluation Indicator

The valuation indicators used to evaluate the results are: mean error  $m$ , root mean square error (RMSE)  $r$ , correlation coefficient  $\rho$ , and accuracy  $\alpha$ . The indicators are defined as follows

$$m = \frac{1}{K} \sum_{k=1}^K \tilde{h}_k - h_k \quad (33)$$

$$r = \sqrt{\frac{1}{K} \sum_{k=1}^K (\tilde{h}_k - h_k)^2} \quad (34)$$

$$\rho = \frac{\text{Cov}(\tilde{h}, h)}{\sqrt{\text{Var}(\tilde{h})\text{Var}(h)}} \quad (35)$$

$$\alpha = \frac{1}{K} \sum_{k=1}^K I_{|\tilde{h}_k - h_k| < \sigma} \quad (36)$$

where Cov is the covariance function and Var is the variance function.  $I_{|\tilde{h}_k - h_k| < \sigma}$  is the indicative function defined as flows

$$I_{|\tilde{h}_k - h_k| < \sigma} = \begin{cases} 1, & \text{if } |\tilde{h}_k - h_k| < \sigma \\ 0, & \text{otherwise.} \end{cases} \quad (37)$$

#### 4.3. Forest Height Inversion

Part 1 in Figure 1 illustrates the processing flowchart. The preprocessing includes coregistration, flat-ground phase removal, geocoding, and coherence estimation. The coregistration has been performed by DLR [45]. The flat-ground phase removal can be completed according to the flat-ground phase files. After the flat-ground phase removal, the coregistered image can be converted into geocoded geometry using conversion matrices, which are included in the master products. The coherences are calculated using a boxcar filtering, with a sliding window size of  $7 \times 7$ . The boxcar filtering can reduce the speckle noise of SAR images and the output pixel value is an average of pixels in the sliding window.

Since the resolution of the LiDAR data is different from that of the PolInSAR forest map, an interpolation is processed on LiDAR data to better compare the inversion results. The bicubic interpolation [48] is performed to generate a more reasonable interpolation result. Specifically, the output pixel value is a weighted average of pixels in the nearest  $4 \times 4$  neighborhood. If there is no particular illustration in the following text, the LiDAR H100 has been interpolated.

To facilitate the further analysis of the two iterative algorithms, four sets of comparative experiments are implemented at both bands, respectively. Concretely, the experimental configurations are carried out, i.e., (a) TSIA + EBCR + LUT, (b) TSIA + IEBCR + ILUT, (c) TSIA + EBCR + ILUT, and (d) TSIA + IEBCR + LUT. Note that all the configurations follow the same processing flow shown in Figure 1. The difference between IEBCR and EBCR is whether using the relationship between the eigenvectors of adjacent points on the boundary. Moreover, the power methods are used to obtain the eigenvector in the extraction of BCR, and the termination condition of the power methods is identical. At the same time, the step size of height and extinction in the ILUT and LUT is the same.

#### 4.4. Forest Height Validation

As shown in Figure 8b, 105 polygons over the entire test site are selected from the original LiDAR H100 to provide validation for the estimated height. To reduce the influence of topographic variation, each individual polygon is selected only from the homogenous areas. For better validation, all the estimated heights were transformed from slant range geometry to the UTM Zone 34 coordinate.

##### 4.4.1. P-Band

Figure 9 provides the inversion height maps from P-band data. All the color ramps range from 0 to 35 m for convenient comparisons with the LiDAR H100. The influence of IEBCR and ILUT on the inversion accuracy can be obtained from the following comparisons. Concretely, the difference between IEBCR and EBCR can be obtained from Figure 9a,d. The difference between ILUT and LUT can be acquired from Figure 9a,c. The total influence of IEBCR and ILUT can be seen from Figure 9a,b. The estimated heights of the four sets of experiments are almost the same in terms of visual effects. It demonstrates that the proposed iterative algorithms almost have no deterioration on the inversion results. To further evaluate the estimated heights, the mean value of each polygon is calculated from the LIDAR H100 and the Pol-InSAR estimated height separately. The correlation plots and the evaluation indicators in 105 polygons are shown in Figure 10. As shown in Figure 10a, the inversion heights from TSIA + EBCR + LUT reach the mean error of  $-2.08$  m, the RMSE of 4.92 m, the correlation coefficient of 0.58, and the accuracy of 61.54%. Figure 10b–d show the similar indicators.

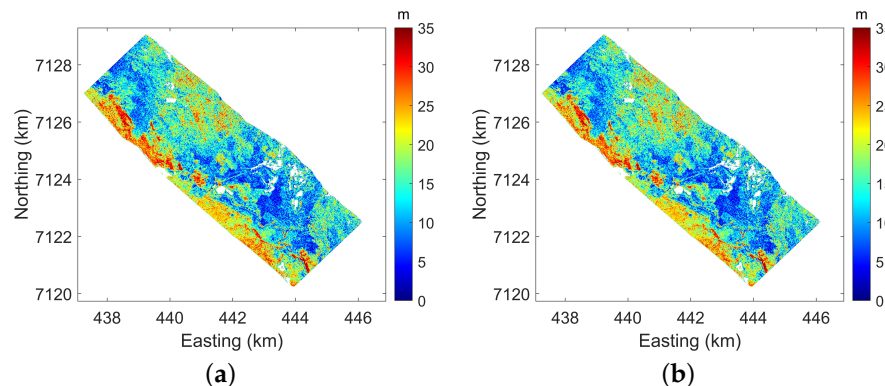


**Figure 9. Cont.**

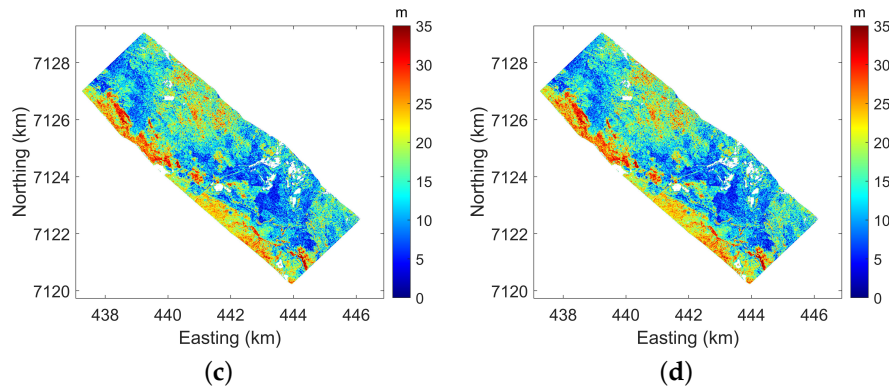


**Figure 9.** The forest height inversion results of P-band in different configurations. The color ramps ranges from 0 to 35 m. (a) TSIA + EBCR + LUT. (b) TSIA + IEBCR + ILUT. (c) TSIA + EBCR + ILUT. (d) TSIA + IEBCR + LUT.

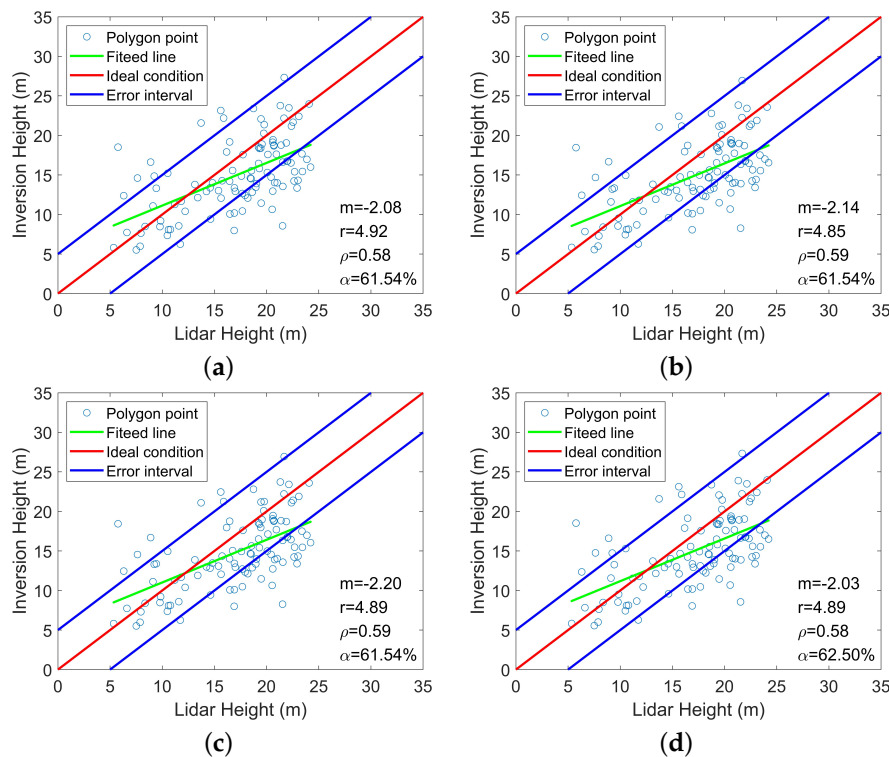


**Figure 10.** The correlation plots of P-band in different configurations. (a) TSIA + EBCR + LUT. (b) TSIA + IEBCR + ILUT. (c) TSIA + EBCR + ILUT. (d) TSIA + IEBCR + LUT.

#### 4.4.2. L-Band

Figure 11 shows the inversion height maps from L-band data and Figure 12 presents the comparisons and the evaluation indicators in polygons. The similar inversion results in Figure 11a–d indicates that the iterative methods are also valid at L-band. As shown in Figure 12a, the inversion heights from TSIA + EBCR + LUT reach the mean error of 0.99 m, the RMSE of 4.22 m, the correlation coefficient of 0.73, and the accuracy of 78.10%. Figure 12b–d show the similar indicators.

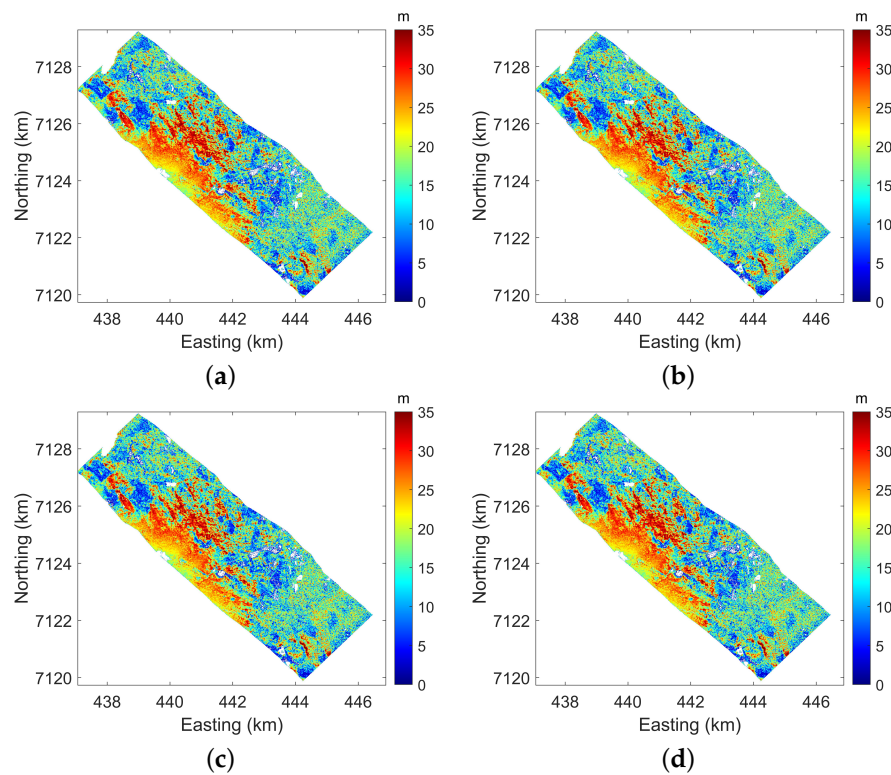


**Figure 11.** The single baseline inversion results of L-band in different configurations. The color ramps = [0, 35] m. (a) TSIA + EBCR + LUT. (b) TSIA + IEBCR + ILUT. (c) TSIA + EBCR + ILUT. (d) TSIA + IEBCR + LUT.

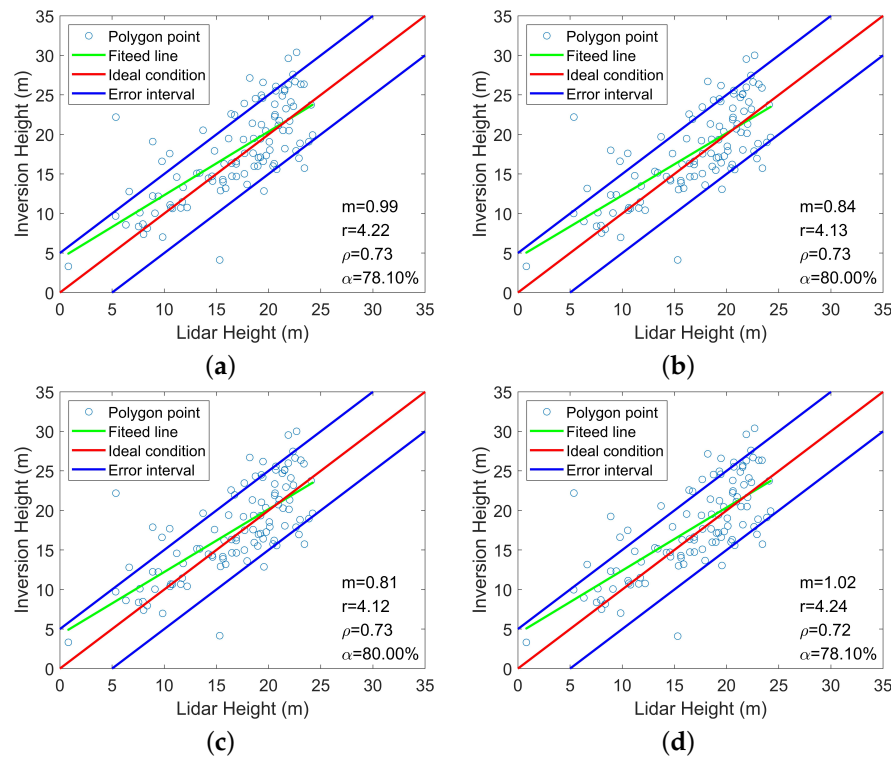


**Figure 12.** The correlation plots of L-band in different configurations. (a) TSIA + EBCR + LUT. (b) TSIA + IEBCR + ILUT. (c) TSIA + EBCR + ILUT. (d) TSIA + IEBCR + LUT.

## 5. Discussion

### 5.1. Quality of Forest Height Estimation

For both bands, the indicators of the estimated height maps from different experimental configurations are quite similar. The L-band inverted heights correlated better with LiDAR H100 than that of the P-band. As shown in Figures 10 and 12, the height estimates at P-band suffer a more serious underestimation than L-band. The main reason may be interpreted from the stronger penetration from P-band. First, the ground contribution in all polarimetric channels makes the estimation of the volume-only coherence a challenge. Although  $\gamma_h$  is regarded as the best candidate for volume-only coherence, the GVR still cannot be neglected. Second, the strong penetration introduces more uncertainty in the sorting of GVR at different polarization channels, which makes Equation (8) fail, resulting in the wrong choice of  $\gamma_h$  and ground phase.

### 5.2. Analysis of IEBCR

#### 5.2.1. Analysis of the Accuracy

To better evaluate the accuracy of the IEBCR, we compare the inversion results from different experiment configurations. Specifically, we analyzed the results from TSIA + IEBCR + ILUT and TSIA + EBCR + ILUT. Figure 13 presents their absolute difference of estimated heights. As shown in Figure 13c, most areas show a difference smaller than 1 m at both bands. In the valid areas, the difference is equal to 0 in 63% of the pixels at P-band and 75% at L-band. The comparisons illustrate that the IEBCR achieves almost the same inversion results.

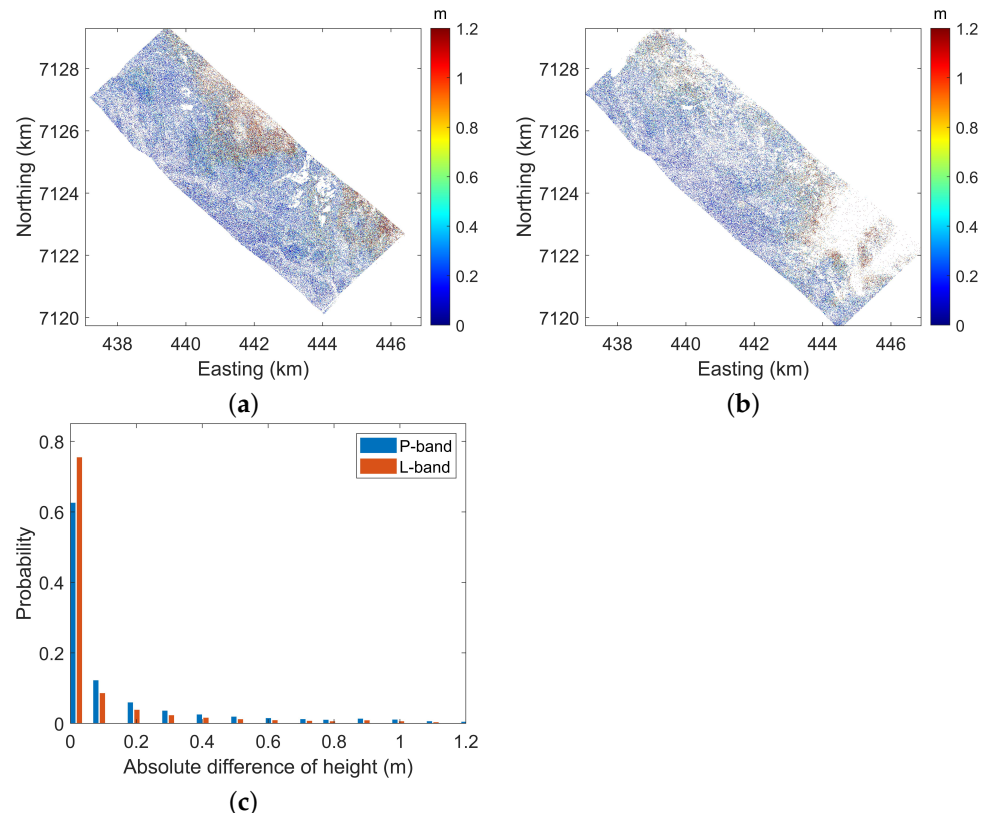


**Figure 13.** The absolute difference of estimated height between TSIA + IEBCR + ILUT and TSIA + EBCR + ILUT. The color ramps range from 0 to 1.2 m. (a) P-band. (b). L-band. (c). The distribution of the absolute difference.

#### 5.2.2. Analysis of Efficiency

The relationship of eigenvectors between adjacent boundary points is changing with the phase spacing. Specifically, the smaller the phase spacing, the closer the eigenvectors.

Furthermore, the closer the eigenvectors, the faster convergence. Therefore, the efficiency should be changed with the number of points on BCR.

To evaluate the efficiency, we performed the Monte Carlo experiments in ECR and IEBCR methods. In the tested area, the power methods are applied to calculate the BCR for each pixel. We set  $N$  in the range of [10, 60] with a spacing of 10. For each  $N$ , the BCR of 1000 pixels is extracted. Figure 14 depicts the average number of iterations in ECR and IEBCR and the improved curve on efficiency. As shown in the figure, the number of iterations in ECR is almost not varied with  $N$ . However, the number of iterations in IEBCR is decreased with the increase of  $N$ . Thus, the improved efficiency rise with the increase of  $N$ . It is consistent with our above analysis. Taking  $N = 30$  in practice provides a good trade-off between accuracy and efficiency.

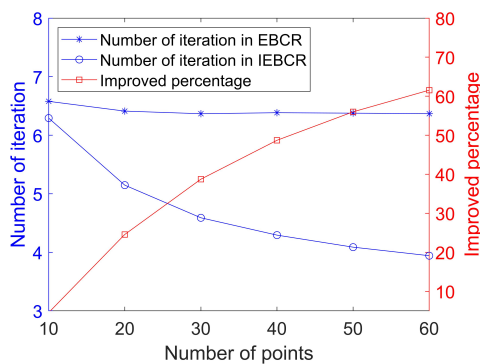


**Figure 14.** The average number of iterations in ECR and IEBCR and the improved curve in efficiency.

### 5.3. Analysis of ILUT

#### 5.3.1. Analysis of the Accuracy

To better evaluate the accuracy of the ILUT, we compare the inversion results from different experiment configurations. Concretely, we analyzed the results from TSIA + IEBCR + ILUT and TSIA + IEBCR + LUT. Figure 15 illustrates the absolute difference of loss between them. The difference is less than 0.01 in more than 99% of the area at both bands. In the numerical calculation, the difference is negligible. The main reason for the error is the height-extinction ambiguity in the interpretation of the interferometric coherence. High forest with a high extinction coefficient generates the same loss function as a low forest with a lower extinction coefficient [28,29].

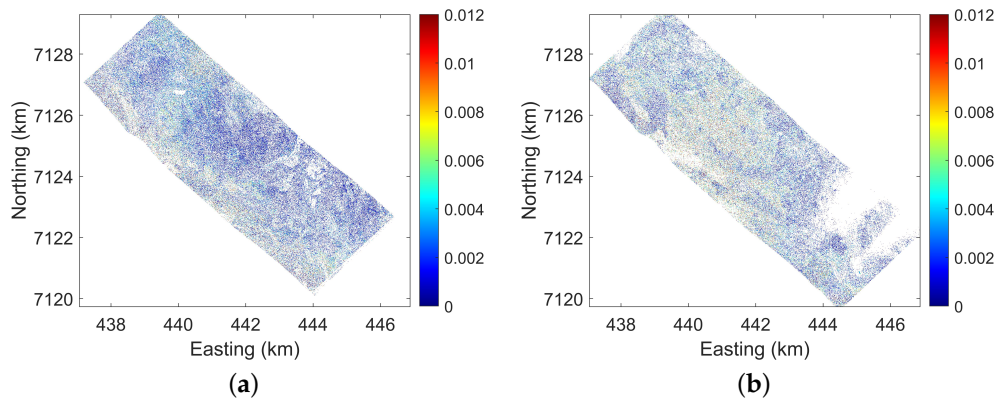


**Figure 15. Cont.**

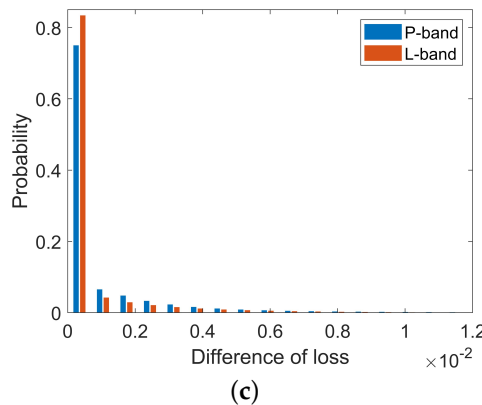


**Figure 15.** The absolute difference of loss function between TSIA + IEBCR + ILUT and TSIA + IEBCR + LUT. (a) P-band. (b) L-band. (c). The distribution of the absolute error.

### 5.3.2. Analysis of the Efficiency

Assuming that the range of  $h_v$  is  $(0, h_{vm})$ , the range of  $k_e$  is  $(0, k_{em})$ , and the precisions are  $\Delta h_v$ ,  $\Delta k_e$ , respectively. The number of the grid points in LUT and ILUT is respectively

$$N_{LUT} = \frac{h_{vm}}{\Delta h_v} \cdot \frac{k_{em}}{\Delta k_e} \quad (38)$$

$$N_{ILUT} = \frac{h_{vm}}{\Delta h_{v1}} \cdot \frac{k_{em}}{\Delta k_{e1}} + (q - 1) \cdot (2m + 1)^2 \quad (39)$$

where  $\Delta h_{v1}$  and  $\Delta k_{e1}$  is the precision in the first search grid of ILUT,  $q$  represents the total number of iterations,  $(2m + 1)^2$  is the number of the grid points in the second and subsequent iterations.

In the inversion process, the consumed time to calculate the coherence based on the model and to search the minima in the grid are linearly dependent on the number of grid points. Therefore, the ratio of the computational complexity can be written approximately as

$$\beta = \frac{N_{LUT}}{N_{ILUT}} = \frac{\frac{h_{vm}}{\Delta h_v} \cdot \frac{k_{em}}{\Delta k_e}}{\frac{h_{vm}}{\Delta h_{v1}} \cdot \frac{k_{em}}{\Delta k_{e1}} + (q - 1) \cdot (2m + 1)^2} \quad (40)$$

We carry out two sets of experiments to verify the above theoretical analysis. In the first experimental configuration, we set  $\Delta h_v = 0.01$  m,  $\Delta k_e = 0.01$  dB/m,  $\Delta h_{v1} = 1$  m,  $\Delta k_{e1} = 0.1$  dB/m,  $q = 3$  and  $k_{em} = 1$  dB/m. In the second case, we set  $\Delta h_v = 0.1$  m,  $\Delta k_e = 0.01$  dB/m,  $\Delta h_{v1} = 1$  m,  $\Delta k_{e1} = 0.1$  dB/m,  $q = 2$ , and  $k_{em} = 1$  dB/m. With these fixed parameters, the ratio of computational complexity relies on the  $h_{vm}$ . We set  $h_{vm}$  in the range of 20–50 m with a spacing of 5 m. For each value of  $h_{vm}$ , 1000 observed coherences are calculated by Equation (6), where the height and extinction are randomly sampled in their respective ranges. Then, we apply LUT and ILUT respectively and record the ratio of consumed time.

Figure 16 provides the theoretical and simulated complexity ratio. Although there are differences between them, the trends of the curves demonstrate a good correspondence. In programming, the vectorized and parallel strategies may affect the actual ratio of consumed time, but the theoretical analysis ensures that the ILUT significantly improves the computational efficiency.

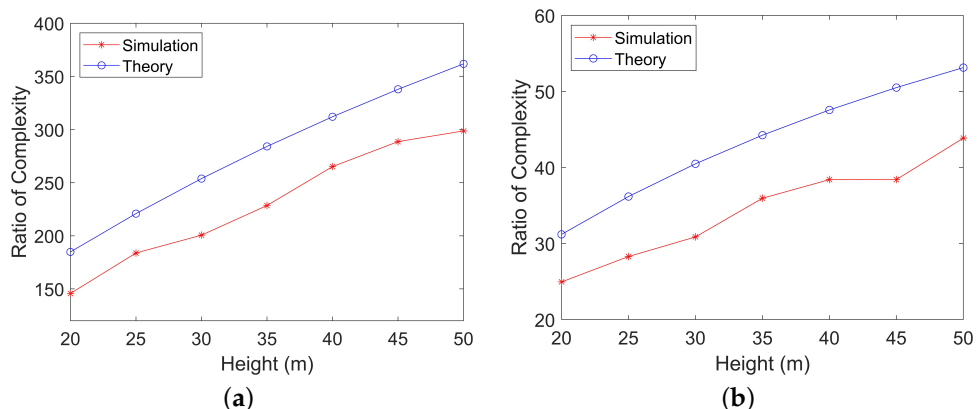


**Figure 16.** Comparison of the ratio of complexity between theoretical analysis and simulation. (a) First experimental configuration. (b) Second experimental configuration.

#### 5.4. Limitations of the Proposed Methods

From the results discussed above, even if IEBCR improves the efficiency by around 40% ( $N = 30$ ), the efficiency still needs to be further improved in practice for large-scale forest height estimation. The main reason is that the analytical form in Equation (13) is not derived. The relationship of the eigenvectors is complex and needs further study.

#### 6. Conclusions

This study set out to enhance the computational efficiency of EBCR and LUT in the TSIA. The IEBCR and ILUT iterative methods are introduced and analyzed. Given many eigendecompositions in the EBCR, we analyzed the relationship of eigenvectors of the adjacent points on the BCR. The analysis manifests the eigenvectors are close in the Euclidean space. Therefore, we proposed the IEBCR utilizing the relationship of eigenvectors. In the final stage, we define the RVoG function and prove its monotonicity and convergence from the analytical and numerical points of view. The proof indicates that the loss function in the LUT does not exhibit extreme irregular properties. Therefore, we propose the iterative LUT (ILUT) for the inversion stage.

The experiments are carried out to verify the effectiveness of the proposed algorithms based on the BioSAR 2008 PolInSAR data at P- and L-bands. The results demonstrate that

1. The two iterative methods are effective at P- and L-bands in single-baseline forest height inversion.
2. The iterative methods can significantly improve the computational efficiency without compromising on the accuracy and are applicable to various algorithms for retrieval of forest vertical structure based on the RVoG model.

**Author Contributions:** Conceptualization, Z.H.; methodology, Z.H.; software, Z.H.; validation, Z.H. and X.L.; formal analysis, Z.H.; investigation, Z.H., Y.Y., X.L. and H.C.; resources, Z.H., Y.Y., H.C. and X.L.; data curation, Z.H. and H.C.; writing—original draft preparation, Z.H.; writing—review and editing, Z.H. and X.L.; visualization, Z.H., Y.Y., X.L. and H.C.; supervision, Z.H., Y.Y., H.C. and X.L.; project administration, X.L., Y.Y. and H.C.; funding acquisition, X.L. and Y.Y. All authors have read and agreed to the published version of the manuscript.

**Funding:** This work was supported in part by the National Natural Science Foundation of China under Grant 41801356 and in part by the LuTan-1 L-Band Spaceborne Bistatic SAR data processing program under Grant E0H2080702.

**Institutional Review Board Statement:** Not applicable.

**Informed Consent Statement:** Not applicable.

**Data Availability Statement:** The BioSAR 2008 campaign data is available on <https://earth.esa.int/eogateway/campaigns/biosar-2> (accessed on 18 May 2022) via FTP upon submission of a data access request.

**Acknowledgments:** The authors would like to thank the European Space Agency(ESA) for providing the BioSAR 2008 dataset (ESA EO Project Campaign ID 69499).

**Conflicts of Interest:** The authors declare no conflict of interest.

## Abbreviations

The following abbreviations are used in this manuscript:

RVoG	Random Volume over Ground
TSIA	three-stage inversion algorithm
LiDAR	Light Detection And Ranging
PolInSAR	Polarimetric Interferometric Synthetic Aperture Radar
GVR	ground-to-volume amplitude ratio
NGVR	null ground-to-volume amplitude ratio
RMoG	Random-Motion-over-Ground
VTD	volume temporal decorrelation
BCR	boundary of the coherence region
EBCR	extraction of the boundary of the coherence region
IEBCR	iterative extraction of the boundary of the coherence region
LUT	look-up table
ILUT	iterative look-up table
RMSE	root mean square error

## References

1. Toan, T.L.; Villard, L.; Lasne, Y.; Mermoz, S.; Koleck, T. Assessment of tropical forest biomass: A challenging objective for the biomass mission. In Proceedings of the 2012 IEEE International Geoscience and Remote Sensing Symposium, Munich, Germany, 22–27 July 2012; pp. 7581–7584. [[CrossRef](#)]
2. Bergen, K.M.; Goetz, S.J.; Dubayah, R.O.; Henebry, G.M.; Hunsaker, C.T.; Imhoff, M.L.; Nelson, R.F.; Parker, G.G.; Radloff, V.C. Remote sensing of vegetation 3-D structure for biodiversity and habitat: Review and implications for lidar and radar spaceborne missions. *J. Geophys. Res. Biogeosci.* **2009**, *114*, G00E06. [[CrossRef](#)]
3. Le Toan, T.; Quegan, S.; Davidson, M.W.J.; Balzter, H.; Paillou, P.; Papathanassiou, K.; Plummer, S.; Rocca, F.; Saatchi, S.; Shugart, H. The BIOMASS mission: Mapping global forest biomass to better understand the terrestrial carbon cycle. *Remote Sens. Environ.* **2011**, *115*, 2850–2860. [[CrossRef](#)]
4. Agata, H.; Aneta, L.; Dariusz, Z.; Krzysztof, S.; Marek, L.; Christiane, S.; Carsten, P. Forest Aboveground Biomass Estimation Using a Combination of Sentinel-1 and Sentinel-2 Data. In Proceedings of the IGARSS 2018—2018 IEEE International Geoscience and Remote Sensing Symposium, Valencia, Spain, 22–27 July 2018; pp. 9026–9029. [[CrossRef](#)]
5. Lefsky, M.A.; Cohen, W.B.; Parker, G.G.; Harding, D.J. Lidar Remote Sensing for Ecosystem Studies: Lidar, an emerging remote sensing technology that directly measures the three-dimensional distribution of plant canopies, can accurately estimate vegetation structural attributes and should be of particular interest to forest, landscape, and global ecologists. *BioScience* **2002**, *52*, 19–30. [[CrossRef](#)]
6. Pourshamsi, M.; Xia, J.; Yokoya, N.; Garcia, M.; Lavalle, M.; Pottier, E.; Balzter, H. Tropical forest canopy height estimation from combined polarimetric SAR and LiDAR using machine-learning. *ISPRS J. Photogramm. Remote Sens.* **2021**, *172*, 79–94. [[CrossRef](#)]
7. Papathanassiou, K.P.; Cloude, S.R. Single-baseline polarimetric SAR interferometry. *IEEE Trans. Geosci. Remote Sens.* **2001**, *39*, 2352–2363. [[CrossRef](#)]
8. Garestier, F.; Dubois-Fernandez, P.C.; Champion, I. Forest height inversion using high-resolution P-band Pol-InSAR data. *IEEE Trans. Geosci. Remote Sens.* **2008**, *46*, 3544–3559. [[CrossRef](#)]
9. Soja, M.J.; Persson, H.; Ulander, L.M.H. Estimation of forest height and canopy density from a single InSAR correlation coefficient. *IEEE Geosci. Remote Sens. Lett.* **2014**, *12*, 646–650. [[CrossRef](#)]
10. Kugler, F.; Koudogbo, F.; Gutjahr, K.; Papathanassiou, K. Frequency effects in Pol-InSAR forest height estimation. In Proceedings of the European Conference on Synthetic Aperture Radar (EUSAR), Dresden, Germany, 16–18 May 2006; pp. 1–4.
11. Zhao, L.; Chen, E.; Li, Z.; Zhang, W.; Fan, Y. A New Approach for Forest Height Inversion Using X-Band Single-Pass InSAR Coherence Data. *IEEE Trans. Geosci. Remote Sens.* **2021**, *60*, 5206018. [[CrossRef](#)]
12. Sun, X.; Wang, B.; Xiang, M.; Zhou, L.; Jiang, S. Forest Height Estimation Based on P-Band Pol-InSAR Modeling and Multi-Baseline Inversion. *Remote Sens.* **2020**, *12*, 1319. [[CrossRef](#)]
13. Soja, M.J.; Persson, H.J.; Ulander, L.M.H. Modeling and Detection of Deforestation and Forest Growth in Multitemporal TanDEM-X Data. *IEEE J. Sel. Top. Appl. Earth Obs. Remote Sens.* **2018**, *11*, 3548–3563. [[CrossRef](#)]
14. Kugler, F.; Lee, S.; Hajnsek, I.; Papathanassiou, K.P. Forest Height Estimation by Means of Pol-InSAR Data Inversion: The Role of the Vertical Wavenumber. *IEEE Trans. Geosci. Remote Sens.* **2015**, *53*, 5294–5311. [[CrossRef](#)]

15. Wang, X.; Xu, F. A PolInSAR Inversion Error Model on Polarimetric System Parameters for Forest Height Mapping. *IEEE Trans. Geosci. Remote Sens.* **2019**, *57*, 5669–5685. [[CrossRef](#)]
16. Chen, H.; Cloude, S.R.; Goodenough, D.G.; Hill, D.A.; Nesdoly, A. Radar Forest Height Estimation in Mountainous Terrain Using Tandem-X Coherence Data. *IEEE J. Sel. Top. Appl. Earth Obs. Remote Sens.* **2018**, *11*, 3443–3452. [[CrossRef](#)]
17. Askne, J.I.H.; Santoro, M. On the Estimation of Boreal Forest Biomass From TanDEM-X Data Without Training Samples. *IEEE Geosci. Remote Sens. Lett.* **2015**, *12*, 771–775. [[CrossRef](#)]
18. Shi, Y.; He, B.; Liao, Z. An improved dual-baseline PolInSAR method for forest height inversion. *Int. J. Appl. Earth Obs. Geoinf.* **2021**, *103*, 102483. [[CrossRef](#)]
19. Parache, H.B.; Mayer, T.; Herndon, K.E.; Flores-Anderson, A.I.; Lei, Y.; Nguyen, Q.; Kunlumai, T.; Griffin, R. Estimating Forest Stand Height in Savannakhet, Lao PDR Using InSAR and Backscatter Methods with L-Band SAR Data. *Remote Sens.* **2021**, *13*, 4516. [[CrossRef](#)]
20. Chen, W.; Zheng, Q.; Xiang, H.; Chen, X.; Sakai, T. Forest Canopy Height Estimation Using Polarimetric Interferometric Synthetic Aperture Radar (PolInSAR) Technology Based on Full-Polarized ALOS/PALSAR Data. *Remote Sens.* **2021**, *13*, 174. [[CrossRef](#)]
21. Dietterich, T.G. An experimental comparison of three methods for constructing ensembles of decision trees: Bagging, boosting, and randomization. *Mach. Learn.* **2000**, *40*, 139–157. [[CrossRef](#)]
22. Smola, A.J.; Schölkopf, B. A tutorial on support vector regression. *Stat. Comput.* **2004**, *14*, 199–222. [[CrossRef](#)]
23. Lavalle, M.; Hensley, S. Extraction of Structural and Dynamic Properties of Forests From Polarimetric-Interferometric SAR Data Affected by Temporal Decorrelation. *IEEE Trans. Geosci. Remote Sens.* **2015**, *53*, 4752–4767. [[CrossRef](#)]
24. Garestier, F.; Toan, T.L. Forest Modeling For Height Inversion Using Single-Baseline InSAR/Pol-InSAR Data. *IEEE Trans. Geosci. Remote Sens.* **2010**, *48*, 1528–1539. [[CrossRef](#)]
25. García, M.; Saatchi, S.; Ustin, S.; Balzter, H. Modelling forest canopy height by integrating airborne LiDAR samples with satellite Radar and multispectral imagery. *Int. J. Appl. Earth Obs. Geoinf.* **2018**, *66*, 159–173. [[CrossRef](#)]
26. Brigot, G.; Simard, M.; Colin-Koeniguer, E.; Boulch, A. Retrieval of forest vertical structure from PolInSAR data by machine learning using LIDAR-derived features. *Remote Sens.* **2019**, *11*, 381. [[CrossRef](#)]
27. Li, W.; Niu, Z.; Shang, R.; Qin, Y.; Wang, L.; Chen, H. High-resolution mapping of forest canopy height using machine learning by coupling ICESat-2 LiDAR with Sentinel-1, Sentinel-2 and Landsat-8 data. *Int. J. Appl. Earth Obs. Geoinf.* **2020**, *92*, 102163. [[CrossRef](#)]
28. Treuhaft, R.N.; Madsen, S.N.; Moghaddam, M.; Zyl, J.J.v. Vegetation characteristics and underlying topography from interferometric radar. *Radio Sci.* **1996**, *31*, 1449–1485. [[CrossRef](#)]
29. Treuhaft, R.N.; Siqueira, P.R. Vertical structure of vegetated land surfaces from interferometric and polarimetric radar. *Radio Sci.* **2000**, *35*, 141–177. [[CrossRef](#)]
30. Cloude, S.R.; Papathanassiou, K.P. Polarimetric SAR interferometry. *IEEE Trans. Geosci. Remote Sens.* **1998**, *36*, 1551–1565. [[CrossRef](#)]
31. Cloude, S.; Papathanassiou, K. Three-stage inversion process for polarimetric SAR interferometry. *IEE Proc. Radar Sonar Navig.* **2003**, *150*, 125–134. [[CrossRef](#)]
32. Flynn, T.; Tabb, M.; Carande, R. Coherence region shape extraction for vegetation parameter estimation in polarimetric SAR interferometry. In Proceedings of the IEEE International Geoscience and Remote Sensing Symposium, Toronto, ON, Canada, 24–28 June 2002; Volume 5, pp. 2596–2598. [[CrossRef](#)]
33. Mark, T.; Jeffrey, O.; Thomas, F.; Richard, C. Phase diversity: A decomposition for vegetation parameter estimation using polarimetric SAR interferometry. In Proceedings of the European Conference on Synthetic Aperture Radar EUSAR, Koln, Germany, 4–6 June 2002; pp. 721–724.
34. Lavalle, M. Full and Compact Polarimetric Radar Interferometry for Vegetation Remote Sensing. Ph.D. Thesis, Université Rennes 1, Rennes, France, 2009.
35. Colin, E.; Titin-Schnaider, C.; Tabbara, W. An interferometric coherence optimization method in radar polarimetry for high-resolution imagery. *IEEE Trans. Geosci. Remote Sens.* **2006**, *44*, 167–175. [[CrossRef](#)]
36. Lu, H.X.; Song, W.Q.; Li, F.; Wang, Y.H.; Liu, H.W.; Bao, Z.; Huang, H.F. Forest parameters inversion based on nonstationarity compensation and mapping space regularization. *J. Electron. Inf. Technol.* **2015**, *37*, 283–290.
37. Liao, Z.; He, B.; Bai, X.; Quan, X. Improving forest height retrieval by reducing the ambiguity of volume-only coherence using multi-baseline PolInSAR data. *IEEE Trans. Geosci. Remote Sens.* **2019**, *57*, 8853–8866. [[CrossRef](#)]
38. Touzi, R.; Lopes, A.; Bruniquel, J.; Vachon, P. Coherence estimation for SAR imagery. *IEEE Trans. Geosci. Remote. Sens.* **1999**, *37*, 135–149. [[CrossRef](#)]
39. Wold, S.; Esbensen, K.; Geladi, P. Principal component analysis. *Chemom. Intell. Lab. Syst.* **1987**, *2*, 37–52. [[CrossRef](#)]
40. Neumann, M.; Reigber, A.; Ferro-Famil, L. Data classification based on PolInSAR coherence shapes. In Proceedings of the 2005 IEEE International Geoscience and Remote Sensing Symposium, Seoul, Korea, 29 July 2005; Volume 7, pp. 4852–4855. [[CrossRef](#)]
41. Mathias, R. Matrices with positive definite Hermitian part: Inequalities and linear systems. *SIAM J. Matrix Anal. Appl.* **1992**, *13*, 640–654. [[CrossRef](#)]
42. Al-Hawari, M. *Hermitian Part, and Skew Hermitian Part of Normal Matrices*; Istanbul Commerce University: Istanbul, Turkey, 2016; p. 23.
43. Andrilli, S.; Hecker, D. Numerical methods. In *Elementary Linear Algebra*, 4th ed.; Andrilli, S., Hecker, D., Eds.; Academic Press: Boston, MA, USA, 2010; Chapter 9, pp. 587–643. [[CrossRef](#)]

44. Horn, R.A.; Johnson, C.R. *Matrix Analysis*; Cambridge University Press: Cambridge, UK, 2012.
45. Irena, H.; Rolf, S.; Martin, K.; Ralf, H.; Seungkuk, L.; Lars, U.; Anders, G.; Gustaf, S.; Thuy, L.T.; Stefano, T.; et al. BioSAR 2008 Experiment Final Report. Report, 2009. Available online: [https://earth.esa.int/eogateway/documents/20142/37627/BIOSAR2\\_final\\_report.pdf](https://earth.esa.int/eogateway/documents/20142/37627/BIOSAR2_final_report.pdf) (accessed on 5 May 2022).
46. Laudon, H.; Hasselquist, E.M.; Peichl, M.; Lindgren, K.; Sponseller, R.; Lidman, F.; Kuglerova, L.; Hasselquist, N.J.; Bishop, K.; Nilsson, M.B.; et al. Northern landscapes in transition: Evidence, approach and ways forward using the Krycklan Catchment Study. *Hydrol. Process.* **2021**, *35*, e14170. [[CrossRef](#)]
47. Hajnsek, I.; Kugler, F.; Lee, S.; Papathanassiou, K.P. Tropical-Forest-Parameter Estimation by Means of Pol-InSAR: The INDREX-II Campaign. *IEEE Trans. Geosci. Remote Sens.* **2009**, *47*, 481–493. [[CrossRef](#)]
48. Keys, R. Cubic convolution interpolation for digital image processing. *IEEE Trans. Acoust. Speech Signal Process.* **1981**, *29*, 1153–1160. [[CrossRef](#)]